Preprint Title Mechanical Property Measurements Enabled by Short Term Fourier Transform of Atomic Force Microscopy Thermal Deflection Analysis

Authors Thomas Mathias, Roland Bennewitz and Philip Egberts

Publication Date 02 Jul 2025

Article Type Full Research Paper

Supporting Information File 1 Supplementary Information.pdf; 727.3 KB

ORCID® iDs Roland Bennewitz - https://orcid.org/0000-0002-5464-8190; Philip Egberts - https://orcid.org/0000-0002-3353-4493

Mechanical Property Measurements Enabled by Short Term Fourier Transform of Atomic Force Microscopy Thermal Deflection Analysis

Thomas Mathias[1], Roland Bennewitz[2] and Philip Egberts*[1]

Address: [1]Department of Mechanical and Manufacturing Engineering, University of Calgary, 2500 University Drive NW, Calgary, AB, T2N 1Y6, Canada and [2]INM-Leibniz Institute for New Materials, Campus D2 2, 66123 Saarbrücken, Germany

Email: Philip Egberts - philip.egberts@ucalgary.ca

* Corresponding author

Abstract

Contact resonance atomic force microscopy (CR-AFM) has been used in many studies to characterize variations in the elastic and viscoelastic constants of materials along a heterogeneous surface. In almost all experimental work, the quantitative modulus of the surface is calculated in reference to a known reference material, rather than calculated directly from the dynamics models of the cantilever. We measure the cantilever displacement with very high sampling frequencies over the course of the experiment and capture its oscillations that result from thermal energy. Using short term Fourier transformations (STFT), it is possible to fit the thermal resonance peak of the normal displacement to track the frequency and Q-factor of the cantilever during an experiment, using a similar process to that used to calibrate the normal bending stiffness of cantilevers. With this quantitive data, we have used the dynamic mechanics models relating the contact stiffness of the tip/cantilever pressing into a surface with the oscillation frequency of the cantilever and show that they do not accurately model the experiment. Several material combinations of tip and sample are examined, as well as tip size and cantilever stiffness demonstrate that existing models cannot capture the physics of this problem.

Keywords

atomic force microscopy; contact resonance; highly oriented pyrolytic graphite (HOPG); mechanical property measurements; surface science

Introduction

Atomic force microscopy (AFM) has become an indispensable tool for imaging surface topography on a variety of surfaces [1]. Since the invention of the AFM [2], several other modes of AFM have been developed, including friction force microscopy [3], tapping mode AFM [4], contact resonance AFM (CR-AFM) [5], etc., each providing unique advantages or insights into a surface and the materials that comprise it. Alongside the developments of the experimental technique has been a number of modeling techniques that can be used to bring physical values or interpretation to the data that is collected by the AFM, allowing operators of the technique to compare their measurements across fields [6].

CR-AFM is a technique that was established in 2008 allowing for the measurement of mechanical properties (elastic modulus and viscoelastic modulus) of surfaces [5]. It is particularly useful for the measurement of heterogeneous surfaces, characteristic of composite and biological materials, where understanding the interplay between microstructure and mechanical properties of the constituent materials is critical for the performance of the overall structure. Analytical models for interpreting the vibrational modes of cantilevers were developed prior to the invention of the technique [7,8]. This model or a variation of it is often presented in manuscripts to explain the interpretation of experimental data, but is not used to bring physical meaning to the experimental data. Instead, in almost every example in the literature, the frequency variation is normalized to what is measured on a surface having known mechanical properties [5,9,10].

Alongside the development of CR-AFM and the analytical models that have been used to describe the technique, spectral analysis of the thermal motion in the deflection of AFM cantilevers has shown promise as a lower-cost or less equipment-intensive mechanism to access the dynamic and time-evolving properties of the cantilever [11-13]. In these techniques, the cantilever deflection signal is acquired at rates several times greater than the first normal resonant frequency (typically greater than 1 MHz) for several seconds, as the cantilever is approached, pressed against, and removed from a surface. Primarily, wavelet transformations of the AFM cantilever's deflection signal has been reported that show variations in the cantilever's contact resonant frequency over the course of the experiment that could be linked to mechanical property variations arising from confined fluids that order, etc [11-13]. However, quantitative measurement or conversion of the measured frequency of the AFM cantilever's bending mode, have not realized at this point.

In this manuscript, we bring together the analytical models that describe cantilever oscillations in AFM experiments where a tip is oscillated and pressed into contact with a solid surface [7,8] with the spectral analysis of the thermal motion of the cantilever. By examination of the thermal oscillations of the AFM cantilever, we can make very small perturbations that are sub Ångström in displacement, or much smaller than atomic bonds in our materials. We also avoid disturbance of the medium surrounding the sample, as is done with photo-thermal excitation, without expensive modification to our existing AFM system. Finally, by avoiding using a phase locked loop to track the frequency of the cantilever oscillation, we are able to track the oscillation of the cantilever as it changes from a free out-of-contact to in-contact oscillator. Additionally, spectral analysis allows for the measurement and tracking of all resonant modes simultaneously, which would otherwise require a phase locked loop for each mode that is to be tracked.

To realize these goals, we have conducted AFM experiments on well-characterized surfaces, such as highly ordered pyrolytic graphite (HOPG), and silicon cantilevers. Short term Fourier transforms, rather than wavelet transforms, are used as the mathematical relationship linking the oscillation parameters and AFM cantilever and the spectral resolution required to accurately capture these parameters are well-documented. Then the analytic models used to interpret CR-AFM experiments are outlined. We then present experimental data on several surfaces are analyzed and their alignment with the analytic models are presented.

Methods

Experiment Design

An Agilent Keysight 5500 AFM was used in all experiments with measurements conducted under ambient laboratory conditions of 20-40% humidity. Four samples were analyzed in the experiments: a silicon wafer, freshly-cleaved highly ordered pyrolytic graphite (HOPG), poly(ethylene oxide) (PEO), and polydimethylsiloxane (PDMS). The mechanical properties of these samples are provided in Table 1 below:

Table 1: Mechanical properties of the examined samples. Values for silicon and HOPG are from Refs [14] and [15]. The values for PEO and PDMS were measured using a Hysitron Premier Nanoindenter.

Material	Young's Modulus (GPa)	Poisson's Ratio
Silicon	160	0.3
HOPG	20	0.25
PEO	0.22 ± 0.03	0.5
PDMS	0.0025 ± 0.0002	0.45

Silicon wafers were ultrasonicated in acetone and subsequently again in ethanol for 10 minutes each. HOPG samples were cleaved using the scotch tape method within 30 minutes of beginning an experiment. Finally, the PEO and PDMS samples were not surface treated following their polymerization/deposition. The topography of the surface was measured before acquiring a force versus distance measurement to ensure that these measurements were acquired on clean and flat regions of the substrate. Force versus distance measurements were acquired by moving the sample up and down at a rate of approximately 100 nm/s and recording the cantilever deflection over the course of the measurement. In addition to the AFM's own control software measuring the deflection of the cantilever over the experiment, the cantilever deflection was measured by a National Instruments BNC box (NI-USB-6341) via an unfiltered connection direct from the photodetector at 2.0 MHz and for 1s duration of the experiment, unless otherwise noted. The data from this instrument will be referred to in the paper as the "high-sample rate" data.

Three types of uncoated cantilevers were used all experiments: soft cantilevers with an integrated tip (Nanosensors PPP-CONT), soft tipless cantilevers (Nanosensors TL-CONT), and harder cantilevers with an integrated tip (Nanosensors PPP-NCL). The soft cantilevers have a nominal stiffness in the normal bending direction of 0.2 N/m and the hard cantilevers have a nominal stiffness of 40 N/m. For each cantilever used, in the normal bending direction was determined through the Sader method [16], with the plan-view dimensions and the setback of the tip from the end of the cantilever measured in an optical microscope. To convert the voltage signal measured by the photodetector, the slope of the force versus distance curve generated from the manufacturer's software was determined, having units of V/m. Four different tip materials were used in experiments: conventional silicon cantilevers (Nanosensors PPP-CONT), conductive diamond coated probes (Nanosensors CDT-CONTR), platinum silicide coated probes (Nanosensors PtSi-CONT), and borosilicate glass colloids (Sigma-Aldrich 440345-100G) attached to the tipless cantilevers (Nanosensors TL-CONT). The borosilicate glass colloids had a diameter of 8-11 µm and an elastic modulus of 60 GPa.

Data Analysis

Following completion of experiments, post processing of the high sample rate data was performed. This data was windowed into segments of data having length of 2^N in number of data points, with N ranging from 10-20. These windowed segments were convolved with the Hanning window to reduce spectral leakage. For each window, a Fourier transform was calculated and stored. Subsequently, for each window generated the resonant peak of the first normal mode was fit using eq. (1),

$$A(f) = \frac{k_B T f_n^3}{\pi Q_n D_n (f^2 - f_n^2)^2 + (\frac{f f_n}{Q_n})^2} \cdot 10^{18} + y_0 \tag{1}$$

where f is the frequency, T is the temperature, $k_B = 1.3806 \times 10^{-23}$ m^{2}kg·s^{-2}K^{-1} is Boltzmann's constant, (Q_n) is the quality factor of the cantilever for the n-th mode, D_n is the stiffness of the n-th oscillation mode, and y_0 is an offset value [17]. Fits of these resonant peaks using the non-linear least squares method yielded parameters f_n, Q_n, and D_n. To ensure accurate fits to the resonance peak, the window size N, impacting the frequency resolution (f_Δ) of the calculated Fourier transform, was carefully chosen to ensure that β in eq. (2) was much larger than 1 [18].

$$\beta = \frac{\pi}{2Q_n}\frac{f_n}{f_\Delta} \tag{2}$$

Fitting of the first resonant peak of the cantilever in contact with the surface during the force versus distance measurement thus provides a time evolution of the f_1, Q_1, and D_1 values as a function of time during the experiments. These values can be related to the displacement of the sample, force, etc. that is time averaged over the window size, thus can be correlated.

Analytical Models of Cantilever Dynamics

Several analytical models of cantilever dynamics have been developed, with the basis of most models originating from the work by Rabe *et al.* in Ref. [7], and are schematically shown in Figure 1 (a) (i) and (ii). More advanced models have been subsequently developed that include the tilt angle of the cantilever relative to the surface [19], to better reflect the typical 12.5° or 22.5° angle of the cantilever relative to the surface, are shown in Figure 1 (a) (iii). To relate the oscillation frequency of the cantilever to the contact stiffness, equations of motion for the schematic have been developed in Refs [7,19]. and are provided in the SI for reference. These equations are used to develop the dispersion curve, shown in Figure 1 (b). The dispersion curve shows how the measured frequency changes as the contact becomes stiffer, which occurs as a result in the previously described experiments by the tip pressing with a larger normal force against the surface. In CR-AFM experiments, typically experiments are conducted at a constant normal force (increasing the tip-sample contact size), and thus changes in the contact stiffness results from variations in the elastic modulus, E, along the surface. The relation between elastic modulus, contact size, and contact stiffness is found in eq. (3) [20],

$$k^* = 2aE^* \tag{3}$$

$$\frac{1}{E^*} = \frac{1 - \nu_{sample}^2}{E_{sample}} + \frac{1 - \nu_{tip}^2}{E_{tip}^*} \tag{4}$$

where a is the size of the contact between the tip and sample, E^* is the reduced elastic modulus defined in eq. (4), ν is the Poisson ratio of the tip or sample, and E is the elastic modulus of the tip or sample.

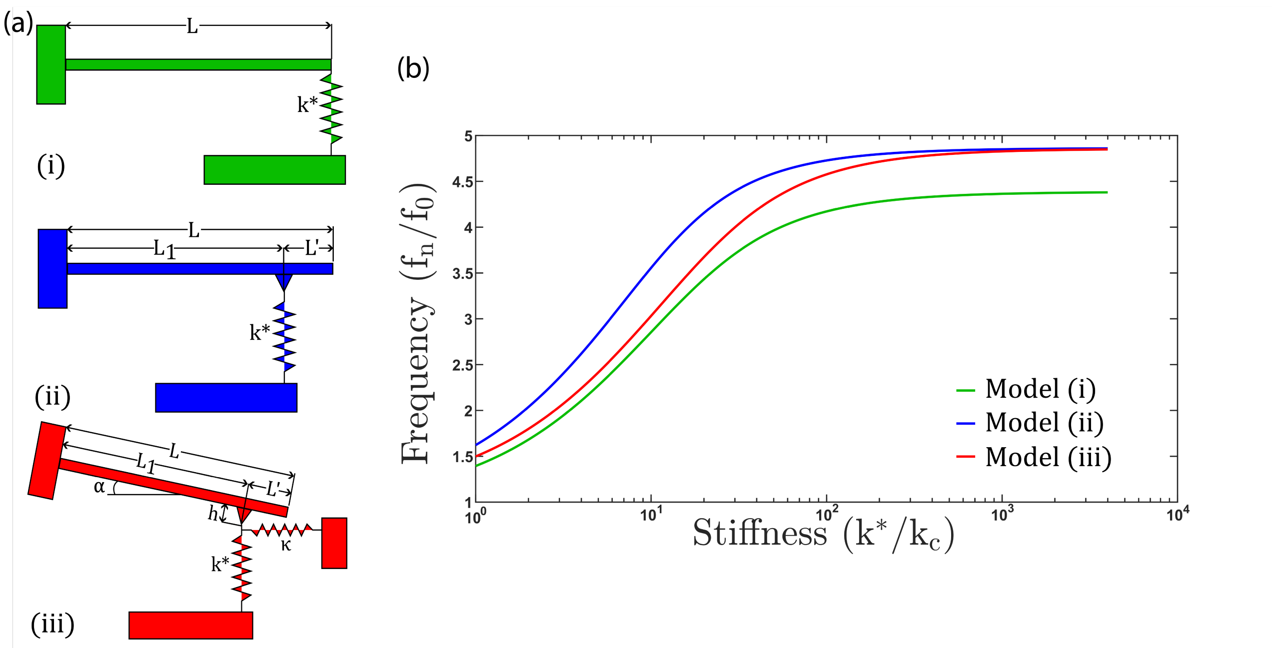

Figure 1: (a) Schematic diagrams of the cantilever models used in determining the dispersion curves to convert measured cantilever oscillation frequency to contact stiffness of the tip-sample contact. Three models are typically used: (i) shows the tip at the end of the cantilever, (ii) shows the tip set back from the end of the cantilever, and (iii) shows a cantilever tilted with respect to the surface and the tip set back from the end of the cantilever. L is the overall cantilever length, L' is the distance that the tip is set back from the end of the cantilever, k^* is the contact stiffness, α is the tilt angle of the cantilever with respect to the surface, h is the distance between the tip apex and the cantilever base, and $\kappa = 8G^*a$ (Ref. [19]) is the lateral stiffness of the tip-sample contact. (b) Dispersion curves providing a lookup table for the conversion of measured resonant frequency to tip-sample contact stiffness. Model (i) is shown in black, (ii) in blue, and (iii) in red.

Results and Discussion

Figure 2 (a) shows an example force versus distance measurement acquired with the high sample-rate acquisition system for a soft silicon cantilever and a HOPG substrate. Both the normal force and cantilever displacement values are shown, as most AFM studies report normal force values, but the power spectrum calculation requires the cantilever displacement values. Figure 2 (b) shows the calculated Fourier transform/power spectrum of the cantilever displacement in the out-of-contact portion of Figure 2 (a), or the data acquired from approximately 0s to 2s of the experiment. The power spectrum clearly shows the first four oscillation modes of the cantilever, with the first oscillation mode having the largest amplitude. Figure 2 (c) shows the quality of the fit obtained using eq. (1) to the first oscillation mode, yielding values of $f_1 = 12.627 \pm 0.003$ kHz, $Q_1 = 19.84 \pm 0.20$, and $D_1 = 25.67 \pm 0.02$ mN/m. We note that the fit value obtained from the eq. (1) is not the the same value as obtained using the Sader method (74.3 mN/m for this cantilever in Figure 2) [16]. Similar observations were made for the other cantilevers used in the experiments conducted within this paper, with the difference between the value of D_1 and the normal spring constant calculated using the Sader method ranging between a factor of 2 and 10. This difference is likely a result of the plan view dimensions of the cantilevers having dimensions beyond the 10% variation of the manufacturer's specifications, observed in other experiments we have conducted outside this study. While viscous damping from the ambient environment is not accounted for in eq. (1) and may also be responsible for a small percentage of the difference between the two calculations of the spring constants, our results highlight that the measurements of the cantilever's plan view dimensions and using these dimensions in the determination of the Sader spring constant or other calculation of the normal spring constant is important. Finally, it has been demonstrated that the Sader method can consistently show a difference compared with the thermal noise method used above, particularly for soft cantilevers as used in this study [21]. We take the Sader spring constant, which has been widely used in other studies and is less sensitive to variations in the calculated cantilever sensitivity [21], as the spring constant of all cantilevers in the calculations in subsequent sections of this manuscript.

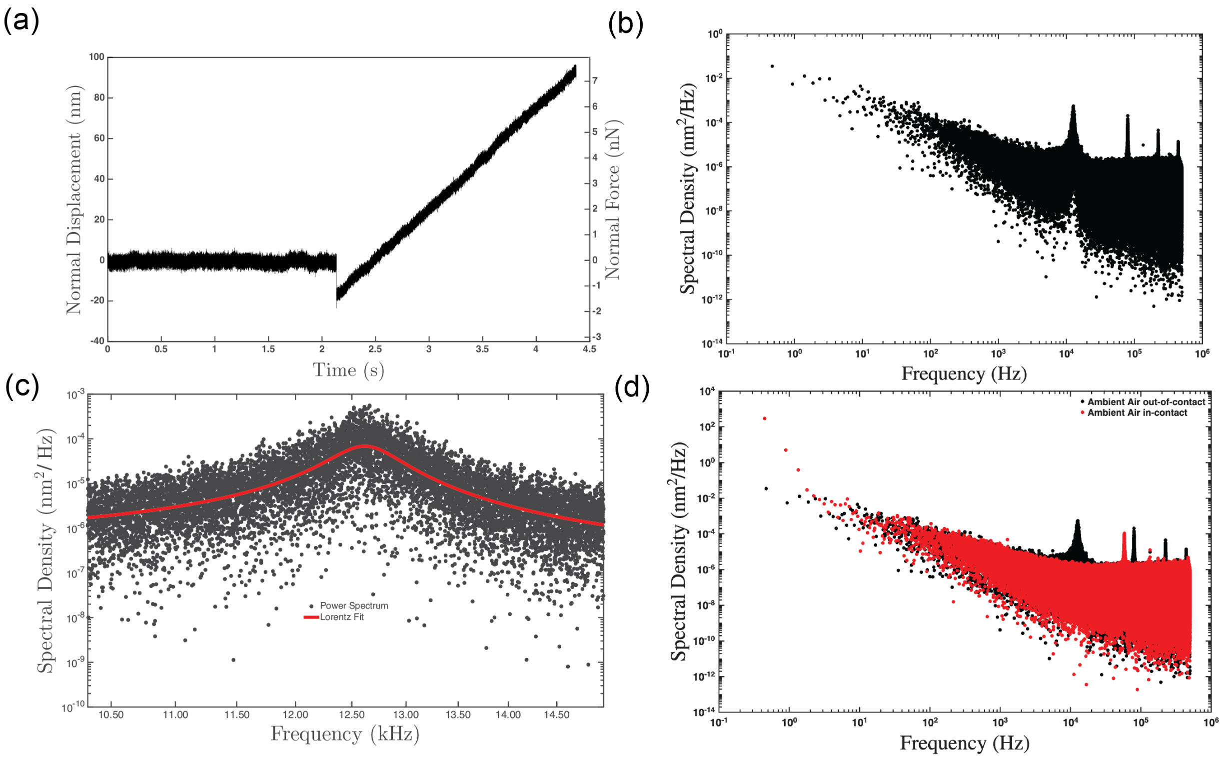

Figure 2: (a) Result of force versus displacement using the high sample rate acquisition system. (b) Fourier transform of the out-of-contact portion of (a). (c) Fit (red line) of the first resonant mode peak (black squares) with eq. (1). (d) Fourier transform of the out-of-contact portion of (a) shown in black and the in-contact portion shown in red, highlighting the change in the resonant peak locations and shapes between these two stages of the measurement. Data was acquired at 1 MHz for approximately 4.5s.

Figure 2 (d) shows two power spectra, the black spectrum calculated from the time ranging from 0s to 2s, and the second in red from the time ranging between 2.5s and 4.5s. These two spectra highlight the change in the location and shape of the normal resonant peaks for the cantilever from when the cantilever was out-of-contact and when it was in contact. We are able to estimate the values of the various modes, as Rabe *et al.* showed that the value of $\frac{f_n}{(k_n L)^2}$ is a constant for the cantilever, which also allows us to distinguish between higher order oscillatory modes of the cantilever and pinning of the free end of the cantilever [7]. With the the first resonant peak out of contact having a center frequency of 12.62 kHz and using Model (i) to estimate the location of subsequent resonant peaks, the expected second resonant mode of a free cantilever would be approximately 79.1 kHz, versus an expected frequency of 55.3 kHz in the first resonant mode if the end of the cantilever was completely pinned. The measured value of the cantilever resonant frequency when the tip was pressed into the surface was 58.15 kHz, which is much closer to the expected value of pinned cantilever than the second resonant mode. Beyond identifying and fitting the first pinned mode of oscillation, it is also possible to observe several of the higher modes within the in-contact power spectrum compared with the out-of-contact spectrum. Finally, we note that the full width at half maximum increases slightly for the first oscillation mode when the cantilever makes contact with the surface, but shows significant scatter during the force curve measurement, making a statement regarding the variation of the Q-factor difficult with the present analysis technique.

Figure 3 (a) shows the variation of the frequency of the first normal mode as a function of normal force during the in-contact portion of the force curve. A sub-linear variation is observed with increasing applied normal force. Figure 3 (b) shows the variation of the quality factor with normal force, simultaneously determined with the frequency of the frequency of the first normal oscillatory mode. Here, the variation in the Q-factor is less clear than for the resonant frequency: an initial increase is observed, that plateaus around 0 nN applied force. However, significant scatter in the Q-factor is observed, in particular compared with the variation in the frequency of the first normal oscillatory mode. Significantly more scatter is observed for the last fit parameter, D_1, which in the case of a free oscillation represents the spring constant of the single-harmonic-oscillator mode. There is significant scatter in the value of D_1 during in-contact measurements, and thus has been included in the SI (Fig. S1) for completeness.

Figure 4 shows the dispersion curves generated for the three cantilever models, with the data obtained from all material combinations evaluated in this study in each of the models. For example, Figure 4 shows that for soft materials, such as the Si-PDMS combination (silicon cantilever, PDMS substrate), all three models can be used to translate the oscillation frequency variation into a contact stiffness. However, for harder materials, such as Si-HOPG or Diamond-Si, Model 1 (Figure 1 (i)) has a frequency response in the dispersion curve that saturates at a reduced frequency (f_1/f_0) that is lower than the measured reduced frequency. Model 3 (Figure 1 (iii))) in this case does not saturate as early, but the plateau in the dispersion curve translates into a wide variation in contact stiffness values assigned for very small changes in frequency. Thus, Model 2 does not have sufficient accuracy for contact stiffness determination for these material systems. Model 2 (Figure 1 (ii)) slightly improves upon this issue, with the dispersion curve shifted more significantly to lower values of contact stiffness and a higher frequency plateau than Model 1, such that improved accuracy in translating the measured cantilever frequency to a stiffness is possible. The additional benefit of Model 2 over Model 3 is that the model is much simpler and a friction coefficient, κ, between the tip/colloid and the substrate does not need to be assumed or calculated to generate the dispersion curve. However, as shown in Figure 1, the value of κ does not significantly change the positioning of the dispersion curve.

It has been suggested that careful selection of the cantilever stiffness is required when performing CR-AFM measurements [22]. Within the context of Figure 1, increasing the value of k_c while all other material parameters remaining constant should shift the measured reduced frequency (f_n/f_0) left or to lower values, to a region of the dispersion curve where a more linear variation between frequency and stiffness is expected. In other words, with a very soft cantilever and a very hard sample, the saturated variation of the reduced frequency changes very little with contact stiffness, k^*. We attempted to use cantilevers with a higher k_c value, ranging from 20-40 N/m to perform the same analysis as done previously. As shown in Fig. S2, the issue becomes that with the stiffer cantilever, the magnitude of the resonance peak for the first normal mode, particularly when the tip contacts the surface, is much smaller than for the softer cantilevers. At this time, the base noise of our AFM system and electronic sampling of the deflection signal is too large to automate the fitting of the resonance peak with reasonable successful fits.

With the frequency data translated to contact stiffness, the DMT, JKR, and Carpick-Ogletree-Salmeron (COS) contact mechanics theories can be used to then relate the tip size, elastic modulus, and normal force. The relationship between contact stiffness, k^*, and normal force for the DMT, JKR, and COS models are then given by eq. (5), eq. (6), and eq. (7), respectively [20,23].

$$k^*_{DMT} = 2E^* \left(\frac{R(3F + F_a)}{4E^*} \right)^{1/3} \tag{5}$$

$$k^*_{JKR} = 2E^* \left(\frac{3R(3F + 2F_a + \sqrt{4FF_a + 4F_a^2})}{2E^*} \right)^{1/3} \tag{6}$$

$$k^*_{COS} = 2E^* \left(\frac{\hat{a}_o}{\hat{F}_c^{1/3}} \right) \left(\frac{R(3F + F_a)}{4E^*} \right)^{1/3} \tag{7}$$

where R is the tip radius and F_a is the adhesive force. In eq. (7), we use the transition parameter, λ, bridge the two contact streams. We then denote $\hat{a}_o = a \cdot \left(\frac{E^*}{\pi\gamma R^2} \right)^{1/3}$ and $\hat{F}_c = \frac{F}{\pi\gamma R^2}$, and γ is the work of adhesion, which can be calculated from the pull-off force in experiments. We calculated the Tabor parameter and the λ-parameter for each material pair and given in Table 2. Rather than fitting data with Tabor parameter less than 0.1 with the DMT model and greater than 5 with the JKR model [24], we use the COS model that has been shown to more accurately fit contacts having material properties between the DMT and JKR extremes. The fits to the experimental data are provided in Figure 5. In each case, all materials for the tip and substrate were pure amorphous/polycrystalline, and thus had homogeneous elastic moduli across the surface. Further, these materials were chosen as they are well-characterized in the literature and often used in AFM experiments. Thus, rather than fitting the elastic modulus of the substrate, we took the elastic modulus values from literature for the tip and substrate and fit the radius of the probes using contact mechanics models. In many cases the fits did not converge, so we have used the best fit values near convergence and plotted the expected model variations for k^* and normal force in Figure 5 in a red dashed line with the experimental data overlayed in the graph. In each case, as stated previously, either the fit did not converge, or yielded unphysical values for the tip radius. More specifically, Figure 5 (a) and (b) show converging fits to the experimental data, resulting in a fit of 0.02580 ± 0.00002 nm and 17.42 ± 0.13 nm, respectively. Figure 5 (c) and (d) show results where the fit did not converge, with the experimental results clearly not following the predicted trend for contact stiffness by the MG model. In these cases the radius estimated for the fit shown in

Figure 5 (c) and (d) was 0.0011 nm and 0.092 nm, respectively. This result is a result of the very high stiffness of the contacting materials that resulted in the reduced frequency having a value near the asymptote of the dispersion curve in Model (ii) and (iii).

Table 2: Tabor and transition parameters calculated for each material pairing.

Probe Material	Sample Material	Tabor μ_T	Transition λ
Silicon	HOPG	0.4567	0.5284
Diamond	Silicon	0.16	0.1851
Glass Colloid	HOPG	7.1923	8.3214
Steel Colloid	Silicon	1.8955	2.1931
Silicon	PEO	3.1962	3.6980
Silicon	PDMS	283.961	328.543

Figure 6 shows SEM images of two of the tips used in the study: a borosilicate glass colloid glued onto a tipless silicon cantilever and a PtSi coated silicon cantilever. In each of these cases, the tip radius was estimated to be much larger than what was fit in Figure 5. While it is possible that, in particular with the colloid probe, local surface roughness will have a much smaller contact radius than the overall probe shape, it is still significantly larger than predicted by the models in Figure 5.

In summary, we have used longstanding analytical models to convert the measured variation in cantilever resonant frequency with applied normal force into contact stiffness. While the measurement process is very similar to what is typically done in CR-AFM studies, it becomes more clear as to why these studies normalize their results to a section or area of the surface with known mechanical properties: the analytical models that have been developed to not accurately describe the variation of cantilever frequency when the tip is pressed against the surface. At this time, no better models were developed to describe the link between cantilever frequency and contact stiffness, and we believe that normalization of the surface properties is the only method that it is possible for experimentalists to provide some understanding of a quantitative value of the surface elastic modulus and other mechanical properties.

Conclusions

High data rate acquisition of the cantilever deflection signal from the photodiode of an AFM allows for the capture of the thermal motion of the AFM cantilever during a force versus distance measurement. STFT analysis was used to produce power spectra at regular time intervals during the experiments, with the frequency resolution varied to balanced against the desire to have a faster time response of the cantilever's oscillation parameters and the necessary frequency resolution to accurately fit the resonant peak of the first normal oscillation mode of the AFM cantilever. The resonance mode was fit to a Lorentz peak to extract its center frequency and quality factor at each time point, providing similar information as to what is generated in a CR-AFM experiment. The cantilever resonant frequency was then converted into contact stiffness using analytical models of cantilever vibrations, which could then be compared with contact mechanics models relating the applied normal force to contact stiffness. It was shown that those commercially available cantilevers, which provide enough signal for analysis in a standard AFM, push CR-AFM into a regime where small variations in frequency result in large variations of derived contact stiffness. This relationship between frequency and contact stiffness makes correlating experimental contact resonance data with contact stiffness, or other mechanical property assessment, very difficult. Thus, our findings show that, while high fidelity data of the changing oscillatory behavior of AFM cantilevers can be obtained with high sampling rates and subsequent STFT analysis, quantitive analysis is not possible without measuring calibration curve or normalizing data on a known material pair. These observations confirm why most CR-AFM studies report normalized data, despite providing information on the analytical models to convert frequency to contact stiffness in most cases, or only show qualitative frequency data.

Acknowledgements

The authors would like to acknowledge funding from the Natural Sciences and Engineering Research Council (NSERC) of Canada Discovery Grants Program (Grant Number RGPIN-2020-04545) and Research Tools and Instruments (RTI), as well as the NSERC Alliance - Alberta Innovates Advance program. The authors would like to acknowledge conversations and support from

Dr. John Sader, Dr. Milana Trifkovic, Dr. Zahra Aboolizadeh, Mr. Nicholas Chan and Dr. Johanna Blass. Finally, the authors would like to thank Dr. Kunal Karan for the use of his AFM.

References

1. Meyer, E.; Hug, H. J.; Bennewitz, R. *Scanning Probe Microscopy: The Lab on a Tip*; Springer-Verlag, 2004.

2. Binnig, G.; Quate, C.; Gerber, C. *Physical Review Letters* **1986**, *56*, 930–933.

3. Mate, C. M.; McClelland, G. M.; Erlandsson, R.; Chiang, S. *Physical Review Letters* **1987**, *59*, 1942–1946.

4. Martin, Y.; Williams, C. C.; Wickramasinghe, H. K. *Journal of Applied Physics* **1987**, *61*, 4723–4729. doi:10.1063/1.338807.

5. Yuya, P. A.; Hurley, D. C.; Turner, J. A. *Journal of Applied Physics* **2008**, *104*, 074916. doi: 10.1063/1.2996259.

6. Szlufarska, I.; Chandross, M.; Carpick, R. W. *Journal of Physics D: Applied Physics* **2008**, *41*, 123001. doi:10.1088/0022-3727/41/12/123001.

7. Rabe, U.; Janser, K.; Arnold, W. *Review of Scientific Instruments* **1996**, *67*, 3281–3293. doi: 10.1063/1.1147409.

8. Yamanaka, K.; Nakano, S. *Applied Physics A* **1998**, *66*, S313–S317. doi:10.1007/s003390051153.

9. Killgore, J. P.; Yablon, D. G.; Tsou, A. H.; Gannepalli, A.; Yuya, P. A.; Turner, J. A.; Proksch, R.; Hurley, D. C. *Langmuir* **2011**, *27*, 13983–13987. doi:10.1021/la203434w.

10. Stan, G.; King, S. W.; Cook, R. F. *Nanotechnology* **2012**, *23*, 215703. doi:10.1088/0957-4484/23/21/215703.

11. Malegori, G.; Ferrini, G. *Nanotechnology* **2011**, *22*, 195702. doi:10.1088/0957-4484/22/19/195702.

12. Pukhova, V.; Banfi, F.; Ferrini, G. *Nanotechnology* **2013**, *24*, 505716. doi:10.1088/0957-4484/24/50/505716.

13. López-Guerra, E. A.; Banfi, F.; Solares, S. D.; Ferrini, G. *Scientific Reports* **2018**, *8*, 7534. doi:10.1038/s41598-018-25828-4.

14. Suk, J. W.; Na, S. R.; Stromberg, R. J.; Stauffer, D.; Lee, J.; Ruoff, R. S.; Liechti, K. M. *Carbon* **2016**, *103*, 63–72. doi:10.1016/j.carbon.2016.02.079.

15. Suriano, R.; Credi, C.; Levi, M.; Turri, S. *Applied Surface Science* **2014**, *311*, 558–566. doi:10.1016/j.apsusc.2014.05.108.

16. Sader, J. E.; Chon, J. W. M.; Mulvaney, P. *Review of Scientific Instruments* **1999**, *70*, 3967. doi:10.1063/1.1150021.

17. Pfeiffer, O.; Loppacher, C.; Wattinger, C.; Bammerlin, M.; Gysin, U.; Guggisberg, M.; Rast, S.; Bennewitz, R.; Meyer, E.; Güntherodt, H. J. *Applied Surface Science* **2000**, *157*, 337–342. doi:10.1016/S0169-4332(99)00548-6.

18. Labuda, A. *Review of Scientific Instruments* **2016**, *87*, 033704. doi:10.1063/1.4943292.

19. Hurley, D. C. *Applied Scanning Probe Methods XI* **2008**, *XI*, 97–138. doi:10.1007/978-3-540-85037-3_5.

20. Johnson, K. *Contact Mechanics*; Cambridge University Press, 1987.

21. te Riet, J.; Katan, A. J.; Rankl, C.; Stahl, S. W.; van Buul, A. M.; Phang, I. Y.; Gomez-Casado, A.; Schön, P.; Gerritsen, J. W.; Cambi, A.; Rowan, A. E.; Vancso, G. J.; Jonkheijm, P.; Huskens, J.; Oosterkamp, T. H.; Gaub, H.; Hinterdorfer, P.; Figdor, C. G.; Speller, S. *Ultramicroscopy* **2011**, *111*, 1659–1669. doi:10.1016/j.ultramic.2011.09.012.

22. Friedrich, S.; Cappella, B. *Beilstein Journal of Nanotechnology* **2020**, *11*, 1714–1727. doi: 10.3762/bjnano.11.154.

23. Carpick, R. W.; Ogletree, D. F.; Salmeron, M. *Journal of Colloid and Interface Science* **1999**, *211*, 395–400.

24. Tabor, D. *Journal of Colloid and Interface Science* **1977**, *58* (1), 2–13. doi:https://doi.org/10.1016/0021-9797(77)90366-6. International Conference on Colloids and Surfaces

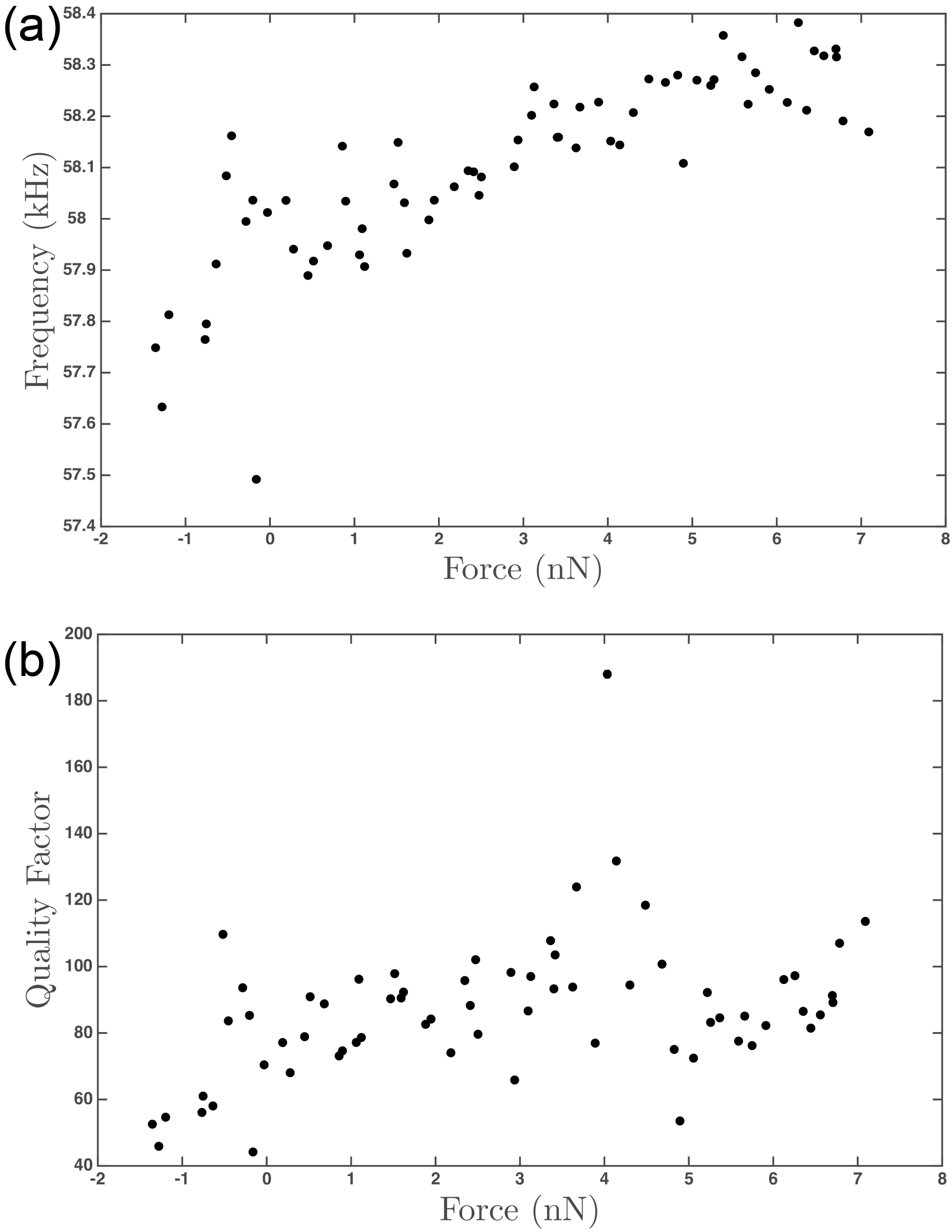

Figure 3: (a) Resonant frequency versus normal force determined from fits of the first normal resonant mode peak in the power spectra of the contact portion of Figure 2. (b) Quality factor (Q) versus normal force similarly determined from the power spectra of the contact portion of Figure 2. N=17 in (a) and (b).

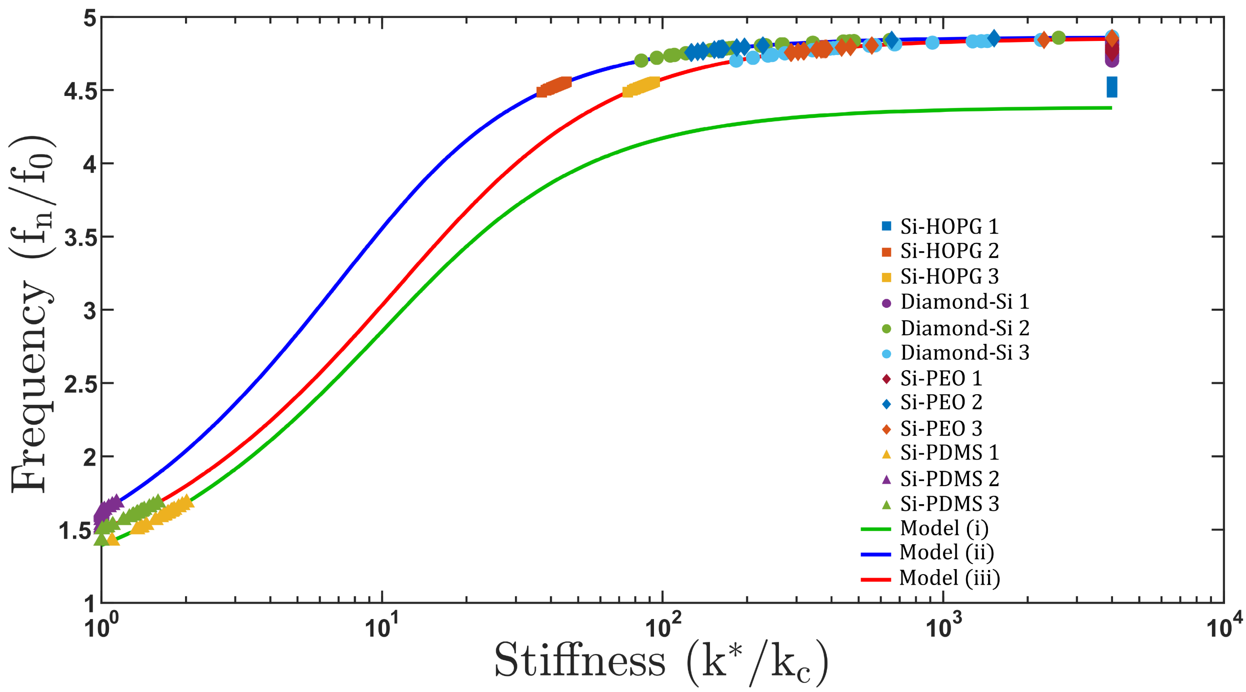

Figure 4: Experimental data for all sample combinations tested (silicon tips vs. HOPG substrate, diamond coated tips on silicon substrate, silicon tip on PEO, silicon tip on PDMS) plotted for the three cantilever models.

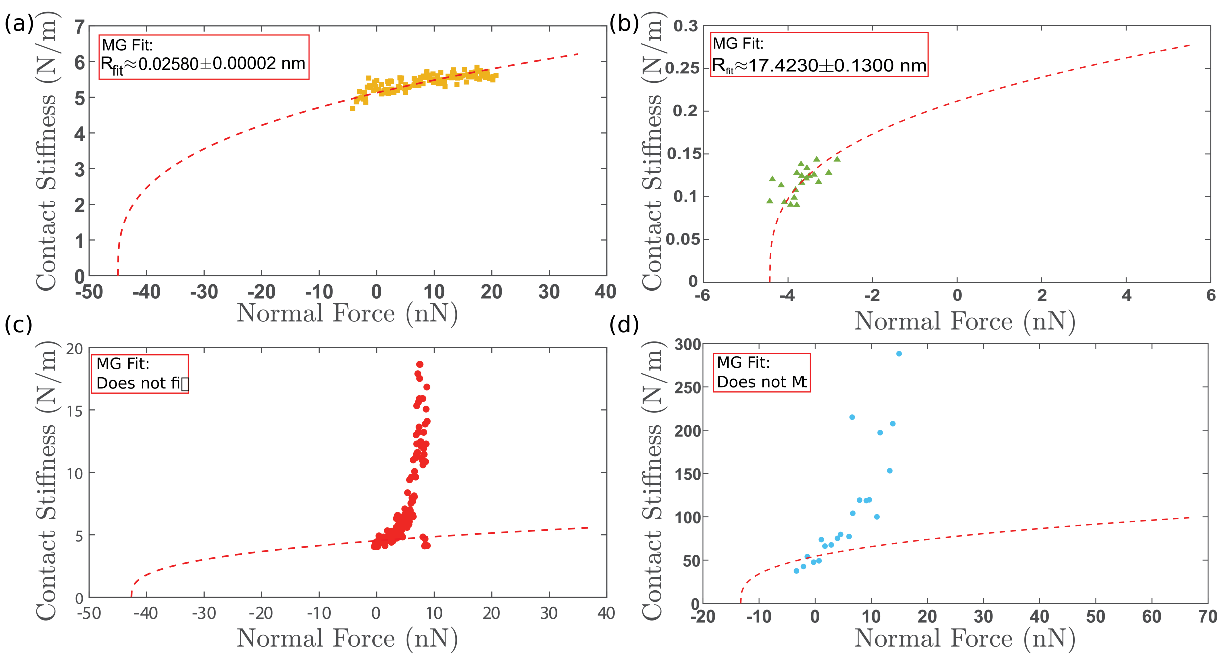

Figure 5: Contact stiffness versus normal force for (a) a silicon probe on HOPG sample (yellow squares) (b) a silicon probe on PDMS sample (green triangles), (c) a borosilicate glass colloid probe on a HOPG sample (red circles), and (d) a diamond coated silicon on silicon sample (blue circles). A red dashed line in each figure shows a fit to the experimental data using eq. (7).

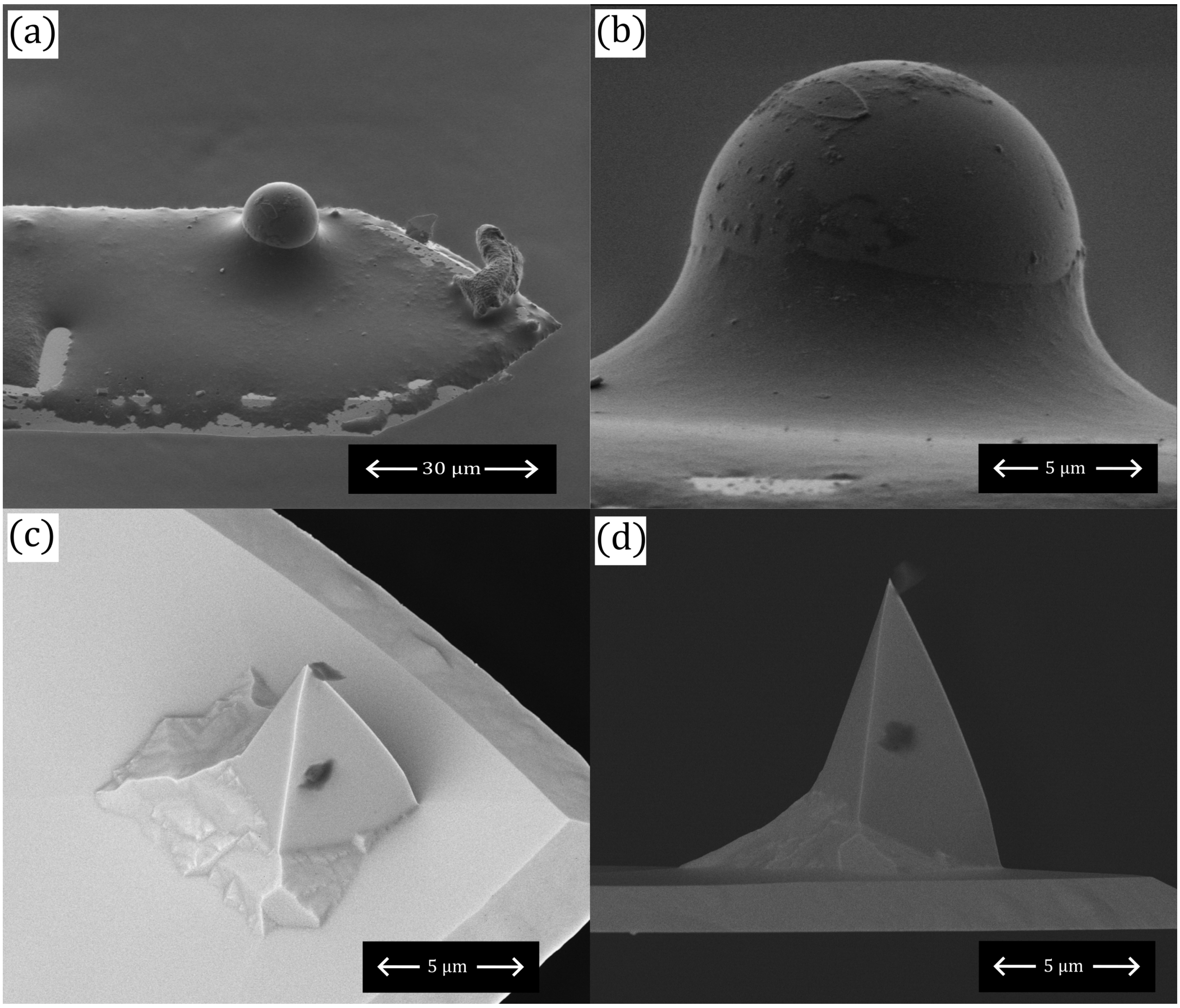

Figure 6: (a) and (b) Scanning electron images of the borosilicate glass colloid glued on the tipless silicon cantilever. (c) and (d) Scanning electron microscope image of PtSi coated AFM cantilever with integrated tip.